




















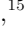
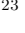







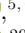




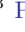







Early results from GLASS-JWST. XVIII: A spectroscopically confirmed protocluster 650 million years after the Big Bang

TAKAHIRO MORISHITA ¹, GUIDO ROBERTS-BORSANI ², TOMMASO TREU ², GABRIEL BRAMMER ^{3,4},
CHARLOTTE A. MASON ^{3,4}, MICHELE TRENTI ^{5,6}, BENEDETTA VULCANI ⁷, XIN WANG ^{8,9}, ANA ACEBRON ^{10,11},
YANNICK BAHÉ ¹², PIETRO BERGAMINI ^{10,13}, KRISTAN BOYETT ^{5,6}, MARUSA BRADAC ^{14,15},
ANTONELLO CALABRÒ ¹⁶, MARCO CASTELLANO ¹⁶, WENLEI CHEN ¹⁷, GABRIELLA DE LUCIA ¹⁸,
ALEXEI V. FILIPPENKO ¹⁹, ADRIANO FONTANA ¹⁶, KARL GLAZEBROOK ²⁰, CLAUDIO GRILLO ^{10,11},
ALAINA HENRY ^{21,22}, TUCKER JONES ¹⁵, PATRICK L. KELLY ²³, ANTON M. KOEKEMOER ²⁴,
NICHIA LEETHOCHAWALIT ²⁵, TING-YI LU ^{3,4}, DANILO MARCHESINI ²⁶, SARA MASCIA ¹⁶, AMATA MERCURIO ²⁷,
EMILIANO MERLIN ¹⁶, BENJAMIN METHA ^{5,6,2}, THEMIYA NANAYAKKARA ²⁰, MARIO NONINO ²⁸, DIEGO PARIS ¹⁶,
LAURA PENTERICCI ¹⁶, PIERO ROSATI ^{29,13}, PAOLA SANTINI ¹⁶, VICTORIA STRAIT ^{3,4}, EROS VANZELLA ³⁰,
ROGIER A. WINDHORST ³¹ AND LIZHI XIE ^{32,18}

¹*IPAC, California Institute of Technology, MC 314-6, 1200 E. California Boulevard, Pasadena, CA 91125, USA*

²*Department of Physics and Astronomy, University of California, Los Angeles, 430 Portola Plaza, Los Angeles, CA 90095, USA*

³*Cosmic Dawn Center (DAWN)*

⁴*Niels Bohr Institute, University of Copenhagen, Jagtvej 128, DK-2200 Copenhagen N, Denmark*

⁵*School of Physics, University of Melbourne, Parkville 3010, VIC, Australia*

⁶*ARC Centre of Excellence for All Sky Astrophysics in 3 Dimensions (ASTRO 3D), Australia*

⁷*INAF Osservatorio Astronomico di Padova, vicolo dell'Osservatorio 5, 35122 Padova, Italy*

⁸*School of Astronomy and Space Science, University of Chinese Academy of Sciences (UCAS), Beijing 100049, China*

⁹*National Astronomical Observatories, Chinese Academy of Sciences, Beijing 100101, China*

¹⁰*Dipartimento di Fisica, Università degli Studi di Milano, Via Celoria 16, I-20133 Milano, Italy*

¹¹*INAF - IASF Milano, via A. Corti 12, I-20133 Milano, Italy*

¹²*Leiden Observatory, Leiden University, P.O. Box 9513, 2300 RA Leiden, The Netherlands*

¹³*INAF - OAS, Osservatorio di Astrofisica e Scienza dello Spazio di Bologna, via Gobetti 93/3, I-40129 Bologna, Italy*

¹⁴*University of Ljubljana, Department of Mathematics and Physics, Jadranska ulica 19, SI-1000 Ljubljana, Slovenia*

¹⁵*Department of Physics and Astronomy, University of California Davis, 1 Shields Avenue, Davis, CA 95616, USA*

¹⁶*INAF Osservatorio Astronomico di Roma, Via Frascati 33, 00078 Monteporzio Catone, Rome, Italy*

¹⁷*School of Physics and Astronomy, University of Minnesota, 116 Church Street SE, Minneapolis, MN 55455, USA*

¹⁸*INAF-Astronomical Observatory of Trieste, via G. B. Tiepolo 11, I-34143, Trieste, Italy*

¹⁹*Department of Astronomy, University of California, Berkeley, CA 94720-3411*

²⁰*Centre for Astrophysics and Supercomputing, Swinburne University of Technology, PO Box 218, Hawthorn, VIC 3122, Australia*

²¹*Center for Astrophysical Sciences, Department of Physics & Astronomy, Johns Hopkins University, Baltimore, MD 21218, USA*

²²*Space Telescope Science Institute, 3700 San Martin Drive, Baltimore, MD 21218, USA*

²³*Minnesota Institute for Astrophysics, University of Minnesota, 116 Church Street SE, Minneapolis, MN 55455, USA*

²⁴*Space Telescope Science Institute, 3700 San Martin Dr., Baltimore, MD 21218, USA*

²⁵*National Astronomical Research Institute of Thailand (NARIT), Mae Rim, Chiang Mai, 50180, Thailand*

²⁶*Physics and Astronomy Department, Tufts University, 574 Boston Avenue, Medford, MA 02155, USA*

²⁷*INAF - Osservatorio Astronomico di Capodimonte, Via Moiariello 16, I-80131 Napoli, Italy*

²⁸*INAF-Trieste Astronomical Observatory, Via Bazzoni 2, I-34124, Trieste, Italy*

²⁹*Dipartimento di Fisica e Scienze della Terra, Università degli Studi di Ferrara, Via Saragat 1, I-44122 Ferrara, Italy*

³⁰*INAF - OAS, Osservatorio di Astrofisica e Scienza dello Spazio di Bologna, via Gobetti 93/3, I-40129 Bologna, Italy*

³¹*School of Earth and Space Exploration, Arizona State University, Tempe, AZ 85287-1404, USA*

³²*Tianjin Normal University, Binshuixidao 393, 300387, Tianjin, China*

Submitted to ApJ Letters

ABSTRACT

We present the spectroscopic confirmation of a protocluster at $z = 7.89$ behind the galaxy cluster Abell 2744. Using JWST NIRSpec, we find six galaxies within a projected distance of 60 kpc, accounting for lensing magnification. We characterize the physical properties of the galaxies via SED fitting of deep HST+JWST imaging data covering 0.4–5.0 μm . Although the galaxies reside in an overdensity around $\sim 130\times$ greater than a random volume, they do not show strong Ly α emission. We place $2\text{-}\sigma$ upper limits on the rest frame equivalent width $< 16\text{--}26\text{ \AA}$. Based on the tight upper limits to the Ly α emission, we constrain the neutral fraction of hydrogen along this line of sight to be $x_{\text{HI}} > 0.45$ (68% CI). Using an empirical $M_{\text{UV}}\text{--}M_{\text{halo}}$ relation for individual galaxies, we estimate that the total halo mass of the system is $\gtrsim 4 \times 10^{11} M_{\odot}$. Likewise, the line of sight velocity dispersion is estimated to be $1200 \pm 300 \text{ km s}^{-1}$. This is the highest redshift spectroscopically confirmed protocluster to date, demonstrating the power of JWST to investigate the connection between dark-matter halo assembly and galaxy formation at very early times with medium-deep observations at < 20 hrs total exposure time. Follow-up spectroscopy of the remaining photometric candidates of the overdensity will further refine the features of this system and help characterize the role of such overdensities in cosmic reionization.

1. INTRODUCTION

Hierarchical structure formation is one of the fundamental features of our standard cosmological model. The first overdensities to collapse and form stars and galaxies play a particularly important role in the evolution of the universe and cosmic reionization (Tegmark et al. 1997). Identifying and studying the sources associated with these first overdensities thus provides critical insights into the evolution of galaxies, the intergalactic medium, and the underlying dark matter scaffolding (e.g., Mo & White 1996).

The clustering of sources around a luminous galaxy or quasar includes an expected excess of fainter companions, under a broad assumption that galaxy luminosity is correlated with the mass of the dark-matter host halo. Such early overdensities are thought to be the seeds of today’s galaxy clusters, and sites where galaxy formation and the evolution of the surrounding gas is progressing more rapidly compared to the mean of the universe. As such, the identification of galaxy overdensities at high redshift ($z > 6$) has been of particular interest in the literature (e.g., Trenti et al. 2012; Castellano et al. 2016, 2018, 2022; Harikane et al. 2019; Tilvi et al. 2020; Endsley & Stark 2022). Furthermore, galaxy overdensities serve as ideal laboratories for studying the ionization of neutral hydrogen around galaxy systems; the presence of a large ionizing bubble may boost the fraction of escaping Ly α photons, which otherwise are scattered and absorbed by surrounding neutral hydrogen (Miralda-Escudé 1998; Dijkstra 2014; Mason & Gronke 2020).

An excess of photometric $z \sim 8$ sources behind the massive galaxy cluster Abell 2744 was discovered in deep HST images taken as part of the Hubble Frontier Fields program (Lotz et al. 2017) and has been

extensively investigated since (Zheng et al. 2014; Atek et al. 2015; Ishigaki et al. 2016). Approximately a dozen photometrically-selected sources are distributed within a small region ($\sim 20''$ across), making it an extreme overdensity, with $\delta \sim 130^{+66}_{-51}$ (Ishigaki et al. 2016), where $\delta = (n - \bar{n})/\bar{n}$ represents the excess of surface number density from the field average.

Spectroscopic follow-up of a number of those sources with VLT/X-Shooter, ALMA, and JWST/NIRISS has secured spectroscopic redshifts for three sources at $z > 7$ (Laporte et al. 2017, 2019; Carniani et al. 2020; Roberts-Borsani et al. 2022a). Of particular interest is the Lyman-break galaxy, YD4, a photometrically-selected member of the protocluster which revealed Lyman- α , [O III] 88 μm , and [C II] 158 μm emission at $z = 8.38$, as well as the presence of dust (Laporte et al. 2017).

Here we report the spectroscopic follow-up and confirmation of the overdensity at $z = 7.89$ (hereafter A2744-z7p9OD), through the detection of the [O III] $\lambda 5007$ line in six member galaxies with JWST/NIRSpec. This result is consistent with the hypothesis that the galaxy confirmed by previous work at $z = 8.38$ is in the background of the protocluster identified here, highlighting the importance of spectroscopic confirmation to establish membership and overdensity, accounting for chance alignment of galaxies sharing similar photometric redshifts.

The cluster field Abell 2744 is the primary target of the GLASS-JWST Early Release Science program (JWST-GO-1324; Treu et al. 2022; Roberts-Borsani et al. 2022a, P.I. Treu), and also part of the JWST Director Discretionary Time program (JWST-GO-2756; P.I. Chen; Roberts-Borsani et al. 2022b) to follow up the discovery of a magnified supernova at $z = 3.47$ (Chen et al. 2022). The wavelength coverage 0.6–5.3 μm af-

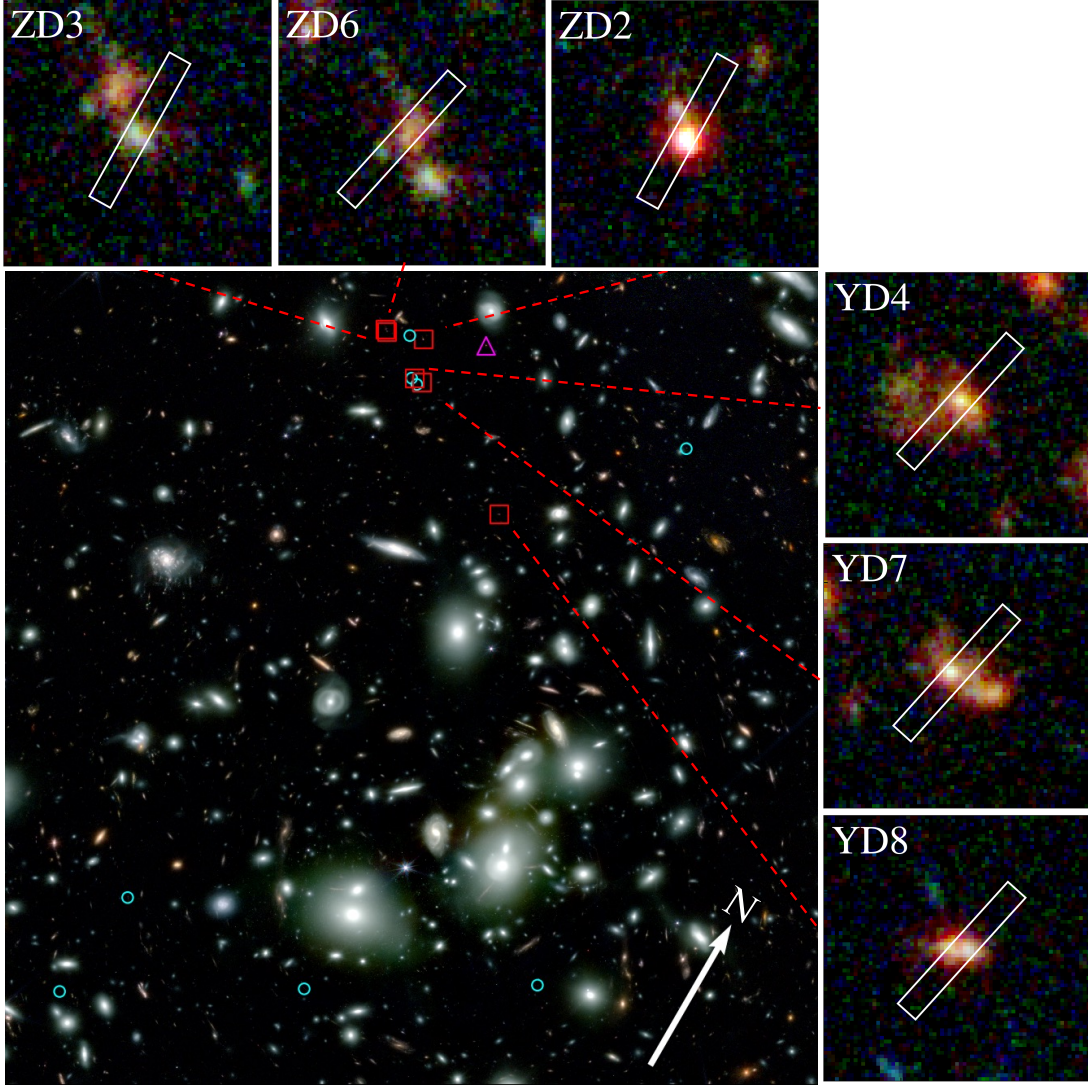


Figure 1. A NIRCам RGB composite image of the Abell 2744 field (blue:F115W, green:F200W, red:F444W). Confirmed galaxies are marked by red squares and shown individually in the zoomed-in panels. The position of the MSA slit for each object is shown (white rectangle). GLASSz8-2 ($z_{\text{grism}} = 7.9$, Roberts-Borsani et al. 2022a) is marked in a magenta triangle. The remaining photometric $z \sim 7.9$ candidates that were originally identified in Zheng et al. (2014) but not covered by our NIRSpec observations, are marked in cyan circles.

forded by the NIRSpec observations not only allows for redshift confirmations of the candidate members via a large suite of emission lines, but also provides insight into the visibility of $\text{Ly}\alpha$ from galaxies in an overdense region. The unique data set is complemented by deep JWST/NIRCам and ancillary HST images, allowing us to characterize the physical properties of the confirmed members and infer the early evolution of galaxies in such an extreme environment. Furthermore, a first estimate of the velocity dispersion of the protocluster can be derived based on the high-precision redshift measurements for individual members.

The paper is structured as follows: we present the data set in Sec. 2, followed by our spectroscopic and

photometric analyses of the cluster members in Sec. 3. We characterize the system and infer the neutral fraction around the system in Sec. 4, and summarize our key conclusions in Sec. 5. Where relevant, we adopt the AB magnitude system (Oke & Gunn 1983; Fukugita et al. 1996), cosmological parameters of $\Omega_m = 0.3$, $\Omega_\Lambda = 0.7$, $H_0 = 70 \text{ km s}^{-1} \text{ Mpc}^{-1}$, and the Chabrier (2003) initial mass function. Distances are in proper units unless otherwise stated.

2. DATA

2.1. JWST/NIRSpec MSA observations

Table 1. Spectroscopically confirmed protocluster galaxies behind Abell 2744

ID	R.A.	Decl.	m _{F150W}	m _{F444W}	Redshift	$f_{H\beta}$	$f_{[OIII]4959+5007}$	EW ₀ (Ly α) [†]
	degree	degree	mag	mag		10 ⁻²⁰ erg/s/cm ²	10 ⁻²⁰ erg/s/cm ²	Å
YD4	3.6038544	-30.3822365	26.5	25.6	7.8761 ^{+0.0001} _{-0.0001}	6.4 ^{+0.8} _{-0.7}	88.6 ^{+2.7} _{-2.7}	< 15.9
YD7	3.6033909	-30.3822289	26.4	25.8	7.8771 ^{+0.0043} _{-0.0053}	< 6.9	18.1 ^{+3.3} _{-2.6}	< 23.9
ZD6	3.6065702	-30.3808918	26.9	26.1	7.8844 ^{+0.0013} _{-0.0013}	< 6.7	25.6 ^{+1.7} _{-1.6}	< 26.2
YD8	3.5960841	-30.3858051	26.7	26.0	7.8875 ^{+0.0003} _{-0.0004}	10.4 ^{+0.7} _{-0.5}	156.8 ^{+3.1} _{-2.9}	< 16.9
ZD2	3.6045184	-30.3804321	26.2	25.2	7.8816 ^{+0.0001} _{-0.0001}	5.2 ^{+0.3} _{-0.3}	30.0 ^{+1.1} _{-1.0}	–
ZD3	3.6064637	-30.3809624	26.7	26.6	7.8761 ^{+0.0001} _{-0.0001}	6.5 ^{+0.8} _{-0.7}	88.4 ^{+2.8} _{-2.9}	–

NOTE—[†] 2 σ rest-frame equivalent width of Ly α over the instrument resolution, $\Delta \sim 100$ Å (~ 2700 km s⁻¹) for PRISM. Ly α equivalent width measurements of ZD2 and ZD3 are not available as the Ly α wavelength falls in the detector gap. Measurements here are not corrected for magnification.

We base our primary analysis on data acquired through NIRSpec MSA observations in two programs, the GLASS-JWST Early Release Science Program (PID 1324, PI Treu; [Treu et al. 2022](#)) and a JWST DDT program (PID 2756, PI. W. Chen; [Roberts-Borsani et al. 2022b](#)). The GLASS-JWST observations were executed on November 10, 2022 with three spectral configurations, G140H/F100LP, G235H/F170LP, and G395H/F290LP, which also provide wavelength coverage of 0.81–5.14 μ m in total, at $R \sim 1000$ –3000. The on-source exposure time was 4.9 hours in each spectral configuration. The DDT NIRSpec observations were executed on October 23 2022, with the CLEAR filter+prism configuration, which provides continuous wavelength coverage of 0.6–5.3 μ m at $R \sim 30$ –300 spectral resolution. The on-source exposure time was 1.23 hours.

For the MSA target selection, we started with the same source catalog for both programs. Specifically for the $z \sim 8$ protocluster sources, z/Y -dropout galaxies (hereafter ZDs and YDs, respectively) were included (4 in the DDT and 4 in GLASS-JWST), all within the vicinity of the overdensity ([Zheng et al. 2014](#); [Ishigaki et al. 2016](#)) including the spectroscopically-confirmed galaxies YD4, GLASSZ8-1 (ZD2) and GLASSZ8-2 from [Laporte et al. \(2017\)](#) and [Roberts-Borsani et al. \(2022a\)](#), respectively. Considering the overlap between the two programs, a total of seven distinct protocluster targets were observed, but data was corrupted for one target due a non-nominal operation of a micro-shutter, leaving six targets suitable for analysis. The choice of protocluster targets in each MSA was based on three primary factors, namely (i) the central pointing of the MSA, (ii) the position of the MSA ensuring no spectral overlap in the detector, and (iii) preferential selection of brighter objects to maximize the probability of emission line or continuum detections.

The data were reduced using the official STScI JWST pipeline (ver.1.8.2)¹ for Level 1 data products, and the `msaexp`² code for Level 2 and 3 data products, the latter of which is built on the STScI pipeline routines but also includes custom routines for additional corrections. Briefly, we begin our data reduction on the uncalibrated files with the `Detector1Pipeline` routine and the latest set of reference files (`jwst_1014.pmap`) to correct for detector-level artifacts and convert to count-rate images. We then utilize custom pre-processing routines from `msaexp` to correct for $1/f$ noise, identify and remove “snowballs”, and remove bias on an exposure-by-exposure basis, before running a number of STScI routines from the `Spec2Pipeline` to produce the final 2D cutout images. These include the `AssignWcs`, `Extract2dStep`, `FlatFieldStep`, `PathLossStep`, and `PhotomStep` routines to perform WCS registration, flat-fielding, pathloss corrections, and flux calibration. Background subtraction is performed locally using a three-shutter nod pattern before drizzling the resulting images onto a common grid. From there, we optimally extract the spectra via an inverse-variance weighted kernel, derived by summing the 2D spectrum along the dispersion axis and fitting the resulting signal along the spatial axis with a Gaussian profile. We visually inspect all kernels to ensure spurious events are not included (or limited) where possible. The kernel then extracts the 1D spectrum along the dispersion axis.

2.2. Imaging data and photometry

Deep NIRCам images are available from DDT program (PID 2756; PI. W. Chen) and GO program UNCOVER (GO 2561; PI I. Labbe), including F115W,

¹ <https://github.com/spacetelescope/jwst>

² <https://github.com/gbrammer/msaexp>

F150W, F200W, F277W, F356W, F410M, and F444W filters. The imaging data are reduced in the same way as presented by [Merlin et al. \(2022\)](#), using the official STScI JWST pipeline, including the most recent version of the photometric zero points and reference files.

To supplement our photometric wavelength coverage, we include ancillary *Hubble* Space Telescope data taken by several programs ([Postman et al. 2012](#); [Treu et al. 2015](#); [Lotz et al. 2017](#); [Steinhardt et al. 2020](#)). The HST data have been uniformly re-reduced using [Grizli](#) ([Brammer et al. 2022](#)).

A photometric catalog is constructed following [Morishita & Stiavelli \(2022\)](#), using [borgpipe](#). Briefly, fluxes are estimated in the PSF-matched images with a $r = 0.''32$ aperture by using [SExtractor](#) ([Bertin & Arnouts 1996](#)). Flux offsets between NIRCcam and HST filters are first corrected with a rescaling based on the mean offset between NIRCcam F150W and a pseudo F150W filter derived for the same sources using the HST F140W and F160W fluxes, whose broad band filters straddle the NIRCcam F150W.

Lastly, fluxes are scaled to a total flux by applying $C = f_{\text{auto},F444W}/f_{\text{aper},F444W}$, where $f_{\text{auto},F444W}$ is FLUX_AUTO of [SExtractor](#), measured for individual sources.

3. ANALYSIS AND RESULTS

3.1. Spectroscopic analysis of $z \sim 8$ candidates

We present our spectroscopic analyses of the six galaxies in our sample in Fig. 2, which shows the two-dimensional spectra and one dimensional extraction. Remarkably, all galaxies show clear [O III] 5007 lines at $\sim 4.4 \mu\text{m}$, and tentative $\text{H}\beta$, [O II], and [Ne III] lines in a few galaxies (see Roberts-Borsani et al., in prep. for a dedicated analysis of the emission lines). Here we focus on redshift determinations using the [O III]-doublet and $\text{H}\beta$ line.

The redshift of each source is determined by fitting a three-component Gaussian to $\text{H}\beta$ and the [O III]-doublet after subtracting the underlying continuum. For the latter, we use a best-fit spectral energy distribution (SED) template derived with broadband photometry (Sec 3.2). We fix the line ratio of the [O III]-doublet lines to 1:3 and set the width to a single parameter for the two components of the doublet. For $\text{H}\beta$, the amplitude and line width are set as free parameters. Including the redshift, we have five free parameters. The uncertainties and parameter posterior distribution functions are estimated via [emcee](#) ([Foreman-Mackey et al. 2013](#)).

In order to assess the detection significance of $\text{H}\beta$ and [O III] emission, we estimate the noise level in the spectrum from $3.6\text{--}4.8 \mu\text{m}$. We measure total fluxes

at various wavelengths integrated over $\pm 2\sigma$ (where σ is the best-fit Gaussian width of each emission line). We then compare the standard deviation of these fluxes (i.e., noise) with the emission lines integrated over $\pm 2\sigma$ around the central wavelength. This test indicates secure ($> 5\sigma$ confidence) detections of [O III] $_{\lambda 5007}$ in all six photometric candidates that were targeted, along with [O III] $_{\lambda 4959}$ in five and $\text{H}\beta$ in three. The resulting line fluxes and spectroscopic redshifts are presented in Table 1. Total line fluxes are measured by integrating the best-fit gaussian component for each line when detected at $> 5\sigma$. The line fluxes and spectroscopic redshifts are presented in Table 1.

3.2. Spectral energy distribution

We analyze the SED of the individual galaxies by using photometric data that covers $0.4\text{--}5 \mu\text{m}$. We use the SED fitting code [gsf](#) ([Morishita et al. 2019](#)), which allows flexible determinations of star formation histories in a non-parametric form, by finding an optimal combination of stellar and interstellar medium (ISM) templates. We generate templates of different ages, [1, 3, 10, 30, 100, 300] Myrs, by using [fspy](#) ([Conroy et al. 2009](#); [Foreman-Mackey et al. 2014](#)). An emission line component that is characterized by an ionization parameter $\log U \in [-3 : 0]$ is also generated by [fspy](#) and added to the template after multiplication by an amplitude parameter. Dust attenuation and metallicity of the stellar templates are treated as free parameters during the fit.

The posterior distribution function of the parameters is sampled by using [emcee](#) for 10^5 iterations with the number of walkers set to 100. The final posterior is collected after excluding the first half of the realizations (known as burn-in). The resulting physical parameters are quoted as the median of the posterior distribution, along with the 16th to 84th percentile uncertainty ranges. The star-formation rate is calculated by averaging the last 100 Myr of the posterior star formation history. The inferred physical properties estimated by our SED analysis are presented in Table 2.

To supplement our characterization of the overdensity (Sec. 4.1), we include the remaining eight photometric candidates presented by [Zheng et al. \(2014, Fig. 1\)](#). As revealed by the spectroscopy, the confirmed sample consists both of ZDs and YDs. The ambiguity is likely due to the fact that the redshift of interest falls in the middle of the effective redshift ranges probed by the two color selections, which define $7 < z < 8$ and $8 < z < 9$ samples, respectively.

We fit the redshifts of the remaining photometric candidates with [EAZY](#) ([Brammer et al. 2008](#)). To exclude possible outliers, we only include those where the 2σ



Figure 2. NIRSpect spectra in the observed wavelength frame (PRISM for the top four and G395H grating for the bottom two) of the confirmed protocluster members. For each galaxy, the top panel shows the 2D and 1D full spectrum; the bottom left panel shows a zoomed region around the Lyman break (blue dashed lines), along with a best-fit template (cyan), where the detector gap region in the G140H grating is masked (gray); the bottom right panel shows the continuum-subtracted spectrum in the region of the $H\beta + [O\text{ III}]$ -doublet lines, where lines with $> 5\sigma$ detection are hatched in yellow. The fitted three-component Gaussian model is also shown (blue). It is noted that the 1D full spectrum in the top panel is resampled to a coarse spectral grid for visualization purposes.

redshift uncertainty overlaps with $z = 7.89$. After this selection, we have nine photometric sources. The SEDs of the selected photometric sources are fitted as described above, with the redshift fixed to $z = 7.89$ (Table 2).

4. DISCUSSION

4.1. Estimate of size, mass, and velocity dispersion of the overdensity

We first investigate the spatial distribution of the member galaxies in A2744-z7p9OD. We use an updated version of the lens model presented by Bergamini et al. (2022) - which includes the recent spectroscopic confirmation of a triply-imaged $z \sim 10$ LBG (Roberts-Borsani et al. 2022b) in the field (Bergamini et al. in prep.) - to correct for the magnification by the foreground cluster. The two-dimensional distribution of our sources in physical units is shown in Fig. 3. After correcting for the lens

magnification, we find that the confirmed sources are located within a circle of radius $R \sim 60$ kpc in the source plane. The distribution on the sky is fairly elongated.

Secondly, we can attempt to estimate the mass of the structure. A detailed mass estimate is challenging to compute since we expect (based on the overdensity factor) that such a protocluster will collapse into a massive cluster by $z = 0$. However, the progenitors of massive clusters are typically spread over several Mpc and thus to estimate the mass of the descendant one would require a survey covering a much larger area of the sky (e.g., Overzier et al. 2009; Contini et al. 2016). Estimating the mass of the structure and its future evolution requires detailed simulations with sufficient resolution and astrophysical detail to resolve individual galaxy components matched in luminosity or stellar mass, while simultaneously probing sufficient volumes to include multiple structures of this kind to average out the expected stochasticity (Chiang et al. 2013), or mapping to a typical dark matter halo rarity then followed across cosmic time (Trenti et al. 2008). This is left for future work.

Following previous work (e.g. Laporte et al. 2022), we can estimate the halo mass of the individual components from the halo-mass galaxy-luminosity relation. Using the relation derived by Mason et al. (2022), we infer that the brightest member of the overdensity (ZD2, $M_{UV} = -20.1$) lives in a $M_h \approx (7 \pm 2) \times 10^{10} M_\odot$ halo. Summing the halo mass of all the confirmed members we obtain a lower limit to the total halo mass $\gtrsim 4 \times 10^{11} M_\odot$.

Lastly, we can take advantage of the spectroscopic data to obtain for the first time an estimate of the velocity dispersion of a protocluster at such high redshift. Given the small number of measured redshifts we adopt a simple Gaussian estimator and bootstrap method to derive the uncertainty (Beers et al. 1990), obtaining $1200 \pm 300 \text{ km s}^{-1}$. We caution the reader that the estimate should be treated with a degree of caution since the system is likely not virialized, and that in computing this quantity we are assuming the spread in redshift with respect to the mean are due to motion as opposed to distance along the line of sight. Nevertheless, we report it to assist future theoretical investigations.

4.2. On the absence of Lyman α emission lines

The absence of strong Ly α emission provides new insight into the intergalactic medium (IGM) properties surrounding the protocluster. None of our spectroscopically confirmed sources shows a clear Ly α line (Fig. 2). To quantify the non-detections, we estimate the upper limit on rest-frame equivalent widths of the line, $\text{EW}_0(\text{Ly}\alpha)$, following Hoag et al. (2019a) and Morishita

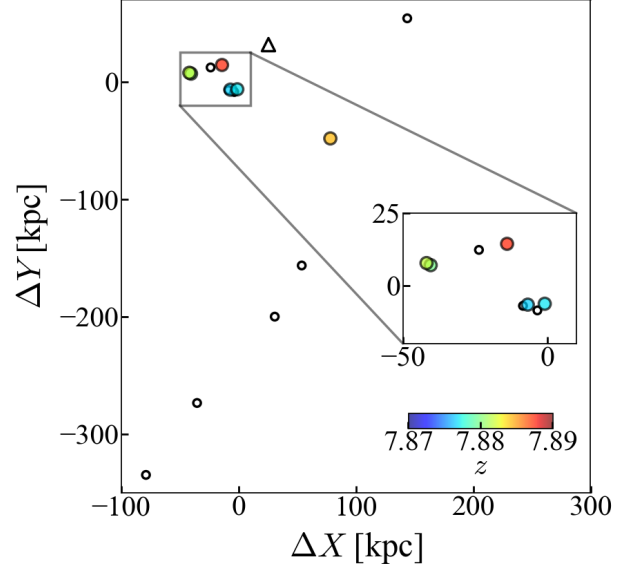


Figure 3. The source plane projected distribution of the confirmed protocluster galaxies (circles, color-coded by spectroscopic redshift), GLASSz8-2 (triangle), and photometric candidates (open circles) in the proper scale. Positions of the galaxies are reconstructed on the source plane. The zoomed-in region around the overdensity is shown in the inset. The zeropoint of the coordinates is set to the centroid of the sources shown here.

et al. (2021):

$$\text{EW}_0(\text{Ly}\alpha) = \frac{F_{\text{Ly}\alpha}}{f_{\text{cont.}}} \frac{1}{(1+z)} \quad (1)$$

For $f_{\text{cont.}}$ we use the continuum model derived from our SED fitting analysis. We replace the non-detected Ly α flux with the limiting flux estimated over the instrumental resolution ($\sim 100 \text{ \AA}$, or 2700 km s^{-1}) at the wavelength of Ly α . The resulting range of upper limits is $\sim 16\text{--}26 \text{ \AA}$ (2σ ; Table 1). The two galaxies (ZD2, ZD3) observed in the ERS programs are not available for the EW measurement as the wavelength range of interest falls in the detector gap.

The lack of strong Ly α emission is perhaps not surprising given the redshift $z = 7.9$ of the host galaxies, where inferences on the ionization state of the IGM find neutral fractions in excess of $x_{\text{HI}} > 70\%$ (Mason et al. 2019; Hoag et al. 2019b). From the measured Ly α EW limits of the four galaxies, and their absolute magnitudes, we estimate the neutral hydrogen fraction along the line of sight to be > 0.45 (at 68% CL) using the same methodology presented by Mason et al. (2018). This is consistent with previous work on the cosmic average, within the uncertainties (Mason et al. 2019). We note that this analysis assumes the observations are independent sightlines. A more realistic analysis including their

correlation within the same physical region would likely recover a slightly lower limit, but is beyond the scope of this work. A larger number of spectroscopic measurements in the protocluster are needed to refine this limit and identify potential differences w.r.t. to the cosmic average.

In such a highly neutral environment large ionized bubbles are expected to be extremely rare (e.g., Mesinger & Furlanetto 2007). Even around regions of comparable overdensity containing sources of similar magnitude ranges, large reionization simulations predict median bubble sizes to be smaller than 1 pMpc where $x_{\text{HI}} > 70\%$ (Lu et al. in prep, using the Evolution of Structure reionization simulations, Mesinger et al. 2016). If the bubble size is below ~ 1 pMpc the redshift along the line of sight is not sufficient for $\text{Ly}\alpha$ to escape, and in fact $\text{Ly}\alpha$ transmission is $\lesssim 20\%$ at its line center (Mason & Gronke 2020). Thus, we expect any emitted $\text{Ly}\alpha$ to be significantly attenuated by the high optical depth in the IGM at this redshift.

We can verify our theoretical expectation by estimating the radius of an H II region, R_{HII} , ionized by UV photons of a single galaxy using the equation in Haiman & Loeb (1997, also Endsley & Stark 2022):

$$\frac{dR_{\text{HII}}}{dt} = \frac{\langle \xi_{\text{ion}} \rangle \langle f_{\text{esc}} \rangle L_{\text{UV}}}{4\pi R_{\text{HII}}^2 \bar{n}_{\text{HI}}(z)} + R_{\text{HII}} H(z) - R_{\text{HII}} \alpha_B \bar{n}_{\text{HI}}(z) \frac{C_{\text{HI}}}{3}. \quad (2)$$

For simplicity, this equation assumes that the ionizing bubble is spherically symmetric and created by a single source at its center. We adopt an ionizing photon production efficiency of $\langle \xi_{\text{ion}} \rangle = 10^{25.8}$ Hz/erg, ionizing photon escape fraction of $\langle f_{\text{esc}} \rangle = 0.2$, a Case B recombination coefficient, $\alpha_B = 2.59 \times 10^{-13}$ cm³/s, and an IGM H I clumping factor $C_{\text{HI}} = 3.0$ (Osterbrock 1989; Shull et al. 2012; Robertson et al. 2013).

By using the derived star formation history and luminosity presented in Sec. 3.2, we estimate the bubble size for the spectroscopically confirmed individual sources and for the photometrically-selected sample identified in Sec. 3.2. The estimated bubble sizes are $\ll 1$ Mpc for most of the sample, due to the relatively low UV luminosity of the galaxies (Table 2). Given that their separation in the source plane is of order 60 pkpc, we also estimate the bubble size by considering the cumulative effect of all the confirmed sources as if they were colocated. Even in this case, we find it to be $R \sim 0.78$ Mpc, i.e. insufficient to allow $\text{Ly}\alpha$ to escape. Even the inclusion of all photometric candidates is not significantly changing the estimate, as those are mostly fainter than

the confirmed members (also see their individual estimates in Table 2).

In conclusion, our bubble size estimate is consistent with the non-detection of $\text{Ly}\alpha$ in our confirmed sources. By comparison, at slightly lower redshifts, Endsley & Stark (2022) estimated bubble sizes of 0.7–1.1 Mpc for UV-bright ($-M_{\text{UV}} \sim 20$ –22 mag) galaxies at $z = 6.6$ –6.9. $\text{Ly}\alpha$ was detected in nine out of ten galaxies, showing that both an overdense environment and sufficient ionizing photon flux is required to produce an ionized bubble large enough to allow significant transmission of $\text{Ly}\alpha$ photons (c.f. the comparison of $\text{Ly}\alpha$ detections in UV-bright and fainter galaxies in Roberts-Borsani et al. 2022c).

4.3. Comparison with previous work

The spectroscopic redshift of the protocluster is in agreement with previous photometric redshift estimates, but in apparent tension with the redshift reported for YD4 ($z = 8.38$) based on $\text{Ly}\alpha$ and ALMA [C II] 158 μm and [O III] 88 μm emission (Laporte et al. 2017, 2019; Carniani et al. 2020). A likely explanation of the apparent tension is a line-of-sight superimposition of sources at similar redshifts. This is a common occurrence in the photometric identification of overdensities and should be kept in mind when considering protocluster candidates without spectroscopy. As shown in Figure 4, YD4 is close on the sky (separation $\sim 0.5''$) to a secondary Y-dropout source (YD6; Zheng et al. 2014), which falls outside our NIRSpect spectroscopic apertures (in the GLASS and DDT observations) but lies within the VLT/X-Shooter long-slit and indistinguishable from YD4 at ALMA resolution (in the case of [C II]). We hypothesize that the source detected at $z = 8.38$ is actually in the background of the protocluster and likely associated with YD6 (estimated to be at $z_{\text{phot}} = 8.3 \pm 0.2$ Zheng et al. 2014). In fact, the [O III] 88 μm flux appears better centered on the fainter counterpart while the detection of dust appears associated with YD4 (see Figure 2 in Laporte et al. 2019), consistent with both the large dust quantity estimated for YD4 in Section 3.2 and the discrepant spectroscopic redshifts. More extensive spectroscopic coverage is needed to confirm the hypothesis.

Our estimated lower limit of the mass of the $z = 7.9$ protocluster is comparable to those of previously known protocluster candidates using similar methods, including the recently reported one behind the SMACS0723 cluster (Laporte et al. 2022). The real breakthrough of our JWST observations, however, is the sheer number of spectroscopically confirmed redshift measurements, which allow us to establish secure membership to the

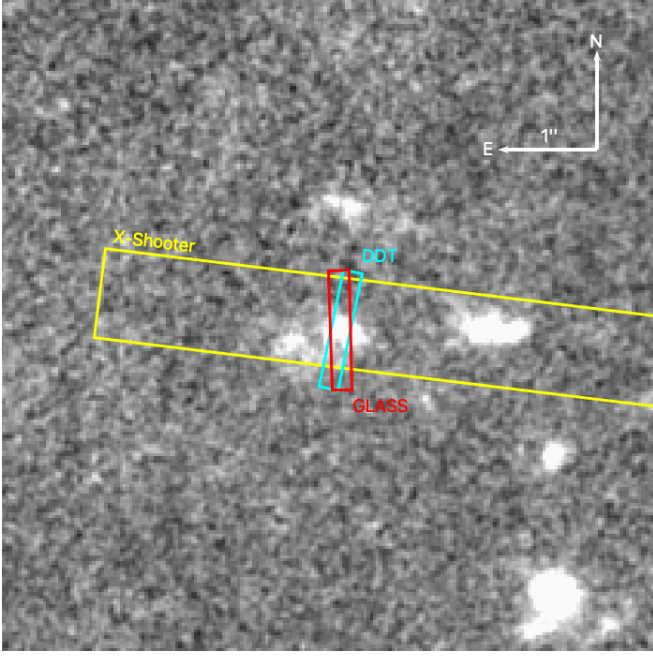


Figure 4. A $5.4'' \times 5.4''$ smoothed F200W NIRCам image centered on YD4, with slits from various programs overlaid. The $\sim 0.2'' \times 1.2''$ NIRSpect/MSA slits from GLASS and the DDT are shown in red and cyan, respectively, while the $\sim 0.9'' \times 11''$ VLT/X-Shooter long-slit from (Laporte et al. 2017) is shown in yellow. The two NIRSpect slits clearly isolate YD4 from a nearby, fainter companion $\sim 0.5''$ South-East of its position, however the X-Shooter long-slit includes both objects.

protocluster and get a first estimate of its velocity dispersion. This clearly provides a glimpse of the power of JWST to add unprecedented detail to studies of the progenitors of today’s large-scale structures.

5. SUMMARY

In this work, we presented a JWST NIRSpect spectroscopic follow-up analysis of six photometrically-selected members of a galaxy overdensity in the epoch of reionization at $z = 7.9$, leading to robust redshift measurements for all photometric candidates by detecting $[\text{O III}]_{\lambda 5007}$ and other rest-frame optical lines. Nine additional photometric candidates identified from new imaging of the field, make A2744-z7p9OD one of the most extreme overdensities in the early universe, with a lower limit on its halo mass of $\gtrsim 4 \times 10^{11} M_{\odot}$. We also obtained a first estimate of the velocity dispersion of the system ($\sigma = 1200 \pm 300 \text{ km s}^{-1}$), which will aid to compare the observations to similar structures identified in cosmological numerical simulations.

While spectroscopic confirmation of the remaining photometric protocluster members is required for further characterization of the overdensity properties, our results clearly show the incredible potential of JWST to confirm $z > 7$ redshifts thanks to the multiplexing capabilities afforded by the NIRSpect MSA. Remarkably, our study reports a 100 % success rate in identifying the redshifts of candidates at high z independently of $\text{Ly}\alpha$, adding a further five confirmed $z > 7$ sources to the literature. Crucially, we refined a previously reported spectroscopic redshift for YD4, suggesting line-of-sight superposition of two distinct sources. This work showcases JWST potential to open a window for determining the properties of galaxies in the early universe. In particular – upon the acquisition of a sufficient sample both in A2744-z7p9OD and field control sample at similar redshift – of particular interest for future progress will be the environmental dependence of physical properties of the sources. In turn, this helps understand the role of galaxy clustering during cosmic reionization.

ACKNOWLEDGEMENTS

We thank Richard Ellis and Nicolas Laporte for useful conversations on the interpretation of the spectroscopic redshift of YD4. Support for program JWST-ERS-1324 was provided by NASA through a grant from the Space Telescope Science Institute, which is operated by the Association of Universities for Research in Astronomy, Inc., under NASA contract NAS 5-03127. KG acknowledges support from Australian Research Council Laureate Fellowship FL180100060. CM and TYL acknowledge support by the VILLUM FONDEN under grant 37459. The Cosmic Dawn Center (DAWN) is funded by the Danish National Research Foundation under grant DNR140. This research is supported in part by the Australian Research Council Centre of Excellence for All Sky Astrophysics in 3 Dimensions (ASTRO 3D), through project number CE170100013. We acknowledge support from the INAF Large Grant 2022 “Extragalactic Surveys with JWST” (PI Pentericci). We acknowledge financial support from grants PRIN-MIUR 2017WSCC32 and 2020SKSTHZ.P MB acknowledges support from the Slovenian national research agency ARRS through grant N1-0238. YMB gratefully acknowledges funding from the Dutch Science Organisation (NWO) under Veni grant number 639.041.751. A.V.F. is grateful for financial support from the Christopher R. Redlich Fund and many individual donors. XW is supported by CAS Project for Young Scientists in Basic Research, Grant No. YSBR-062. RAW acknowledges support from NASA JWST Interdisci-

Table 2. Physical properties of the final candidates.

ID	μ^\dagger	M_{UV}	β_λ	$\log M_*$	SFR	$\log t_*$	$\log Z_*$	A_V	R_{HII}^\dagger
		mag		M_\odot	M_\odot / yr	Gyr	Z_\odot	mag	pMpc
Spectroscopic sample									
YD4	$2.01^{+0.05}_{-0.04}$	$-19.69^{+0.06}_{-0.07}$	$-1.25^{+0.02}_{-0.06}$	$9.22^{+0.16}_{-0.18}$	$7.71^{+2.69}_{-2.39}$	$-1.62^{+0.63}_{-0.45}$	$-1.30^{+0.33}_{-0.33}$	$1.19^{+0.16}_{-0.15}$	$0.01^{+0.01}_{-0.00}$
YD7	$2.02^{+0.05}_{-0.04}$	$-19.93^{+0.05}_{-0.07}$	$-1.85^{+0.02}_{-0.03}$	$9.44^{+0.06}_{-0.14}$	$3.50^{+2.10}_{-1.60}$	$-0.63^{+0.18}_{-0.31}$	$-1.40^{+0.53}_{-0.40}$	$0.32^{+0.16}_{-0.16}$	$0.65^{+0.10}_{-0.14}$
YD8	$2.63^{+0.07}_{-0.06}$	$-19.22^{+0.05}_{-0.04}$	$-2.09^{+0.01}_{-0.05}$	$8.47^{+0.05}_{-0.07}$	$1.72^{+0.22}_{-0.26}$	$-1.44^{+0.15}_{-0.28}$	$-0.36^{+0.17}_{-0.73}$	$0.23^{+0.07}_{-0.04}$	$0.28^{+0.03}_{-0.05}$
ZD6	$1.94^{+0.05}_{-0.04}$	$-19.38^{+0.09}_{-0.09}$	$-1.52^{+0.06}_{-0.08}$	$8.91^{+0.19}_{-0.18}$	$4.45^{+2.04}_{-1.73}$	$-1.47^{+0.35}_{-0.31}$	$-0.93^{+0.82}_{-0.65}$	$0.69^{+0.24}_{-0.20}$	$0.29^{+0.09}_{-0.06}$
ZD2	$1.98^{+0.05}_{-0.04}$	$-20.07^{+0.03}_{-0.02}$	$-2.16^{+0.01}_{-0.02}$	$8.77^{+0.03}_{-0.03}$	$3.52^{+0.22}_{-0.23}$	$-1.49^{+0.17}_{-0.30}$	$-0.30^{+0.03}_{-0.04}$	$0.23^{+0.02}_{-0.01}$	$0.35^{+0.05}_{-0.07}$
ZD3	$1.94^{+0.05}_{-0.04}$	$-19.65^{+0.06}_{-0.07}$	$-2.02^{+0.04}_{-0.05}$	$8.39^{+0.38}_{-0.21}$	$1.01^{+0.63}_{-0.31}$	$-1.38^{+0.67}_{-0.55}$	$-0.80^{+0.68}_{-0.57}$	$0.26^{+0.20}_{-0.13}$	$0.04^{+0.03}_{-0.01}$
GLASSz8-2 ‡	$2.15^{+0.06}_{-0.04}$	$-19.69^{+0.04}_{-0.03}$	$-2.11^{+0.02}_{-0.03}$	$8.60^{+0.04}_{-0.04}$	$2.31^{+0.26}_{-0.19}$	$-1.47^{+0.16}_{-0.28}$	$-0.21^{+0.04}_{-0.08}$	$0.27^{+0.01}_{-0.02}$	$0.31^{+0.04}_{-0.06}$
Photometric sample*									
YD3	$2.79^{+0.08}_{-0.05}$	$-17.54^{+0.17}_{-0.23}$	$-2.07^{+0.13}_{-0.06}$	$7.71^{+0.24}_{-0.25}$	$0.22^{+0.16}_{-0.09}$	$-1.40^{+0.48}_{-0.47}$	$-1.33^{+0.82}_{-0.44}$	$0.38^{+0.31}_{-0.25}$	$0.04^{+0.02}_{-0.01}$
YD6	$2.00^{+0.05}_{-0.04}$	$-18.21^{+0.12}_{-0.16}$	$-1.59^{+0.16}_{-0.04}$	$8.47^{+0.23}_{-0.32}$	$1.60^{+0.97}_{-0.87}$	$-1.28^{+0.33}_{-0.51}$	$-1.10^{+0.87}_{-0.58}$	$0.69^{+0.42}_{-0.36}$	$0.11^{+0.03}_{-0.04}$
ZD1	$2.02^{+0.05}_{-0.04}$	$-17.09^{+0.22}_{-0.37}$	$-1.61^{+0.35}_{-0.12}$	$8.23^{+0.28}_{-0.32}$	$0.82^{+0.82}_{-0.41}$	$-1.35^{+0.34}_{-0.28}$	$-1.21^{+0.77}_{-0.62}$	$0.74^{+0.39}_{-0.48}$	$0.19^{+0.06}_{-0.04}$
ZD4	$1.96^{+0.05}_{-0.04}$	$-17.59^{+0.16}_{-0.19}$	$-1.90^{+0.09}_{-0.04}$	$8.05^{+0.26}_{-0.28}$	$0.62^{+0.54}_{-0.29}$	$-1.37^{+0.31}_{-0.28}$	$-1.02^{+1.05}_{-0.66}$	$0.35^{+0.32}_{-0.20}$	$0.23^{+0.06}_{-0.05}$
ZD5	$3.30^{+0.13}_{-0.13}$	$-17.49^{+0.15}_{-0.18}$	$-2.01^{+0.00}_{-0.06}$	$7.93^{+0.23}_{-0.23}$	$0.43^{+0.29}_{-0.20}$	$-1.30^{+0.42}_{-0.32}$	$-0.54^{+0.35}_{-0.90}$	$0.21^{+0.19}_{-0.14}$	$0.21^{+0.08}_{-0.05}$
ZD7	$10.85^{+0.39}_{-0.38}$	$-20.03^{+0.10}_{-0.12}$	$-2.41^{+0.01}_{-0.00}$	$8.30^{+0.28}_{-0.22}$	$0.85^{+0.68}_{-0.30}$	$-1.51^{+0.65}_{-0.42}$	$-1.39^{+0.48}_{-0.39}$	$0.09^{+0.14}_{-0.07}$	$0.03^{+0.02}_{-0.01}$
ZD9	$4.28^{+0.14}_{-0.11}$	$-17.50^{+0.11}_{-0.15}$	$-2.32^{+0.02}_{-0.12}$	$7.38^{+0.38}_{-0.49}$	$0.11^{+0.15}_{-0.09}$	$-1.29^{+0.52}_{-0.45}$	$-0.04^{+0.33}_{-1.23}$	$0.17^{+0.14}_{-0.12}$	$0.05^{+0.02}_{-0.01}$
ZD10	$6.29^{+0.27}_{-0.34}$	$-15.34^{+0.30}_{-0.46}$	$-1.54^{+0.29}_{-0.12}$	$7.46^{+0.29}_{-0.33}$	$0.09^{+0.11}_{-0.06}$	$-1.08^{+0.44}_{-0.58}$	$-0.58^{+0.64}_{-1.03}$	$0.48^{+0.64}_{-0.34}$	$0.03^{+0.01}_{-0.01}$

NOTE— Median magnification of the lens model by Bergamini (in prep.), calculated at the position of the source. Measurements are associated with 1σ uncertainties. † HII bubble size, calculated with Eq. 2. ‡ Grism redshift $z_{\text{grism}} = 7.90^{+0.1}_{-0.1}$ measured by Roberts-Borsani et al. (2022a). *Sources selected by Zheng et al. (2014) that were not observed in our NIRSpect programs. Only those with photometric redshift consistent with $z = 7.89$ at 2σ are included. Redshift of the photometric sample is fixed to $z = 7.89$ in the SED analysis. All measurements are corrected for magnification.

plinary Scientist grants NAG5-12460, NNX14AN10G and 80NSSC18K0200 from GSFC.

REFERENCES

- Atek, H., Richard, J., Kneib, J.-P., et al. 2015, *ApJ*, 800, 18, doi: [10.1088/0004-637X/800/1/18](https://doi.org/10.1088/0004-637X/800/1/18)
- Beers, T. C., Flynn, K., & Gebhardt, K. 1990, *AJ*, 100, 32, doi: [10.1086/115487](https://doi.org/10.1086/115487)
- Bergamini, P., Acebron, A., Grillo, C., et al. 2022, arXiv e-prints, arXiv:2207.09416, <https://arxiv.org/abs/2207.09416>
- Bertin, E., & Arnouts, S. 1996, *A&AS*, 117, 393
- Brammer, G., Strait, V., Matharu, J., & Momcheva, I. 2022, grizli, 1.5.0, Zenodo, Zenodo, doi: [10.5281/zenodo.6672538](https://doi.org/10.5281/zenodo.6672538)
- Brammer, G. B., van Dokkum, P. G., & Coppi, P. 2008, *ApJ*, 686, 1503, doi: [10.1086/591786](https://doi.org/10.1086/591786)
- Carniani, S., Ferrara, A., Maiolino, R., et al. 2020, *MNRAS*, 499, 5136, doi: [10.1093/mnras/staa3178](https://doi.org/10.1093/mnras/staa3178)
- Castellano, M., Dayal, P., Pentericci, L., et al. 2016, *ApJL*, 818, L3, doi: [10.3847/2041-8205/818/1/L3](https://doi.org/10.3847/2041-8205/818/1/L3)
- Castellano, M., Pentericci, L., Vanzella, E., et al. 2018, *ApJL*, 863, L3, doi: [10.3847/2041-8213/aad59b](https://doi.org/10.3847/2041-8213/aad59b)
- Castellano, M., Pentericci, L., Cupani, G., et al. 2022, *A&A*, 662, A115, doi: [10.1051/0004-6361/202243348](https://doi.org/10.1051/0004-6361/202243348)
- Chabrier, G. 2003, *PASP*, 115, 763, doi: [10.1086/376392](https://doi.org/10.1086/376392)
- Chen, W., Kelly, P., Morishita, T., et al. 2022, *Transient Name Server AstroNote*, 166, 1
- Chiang, Y.-K., Overzier, R., & Gebhardt, K. 2013, *ApJ*, 779, 127, doi: [10.1088/0004-637X/779/2/127](https://doi.org/10.1088/0004-637X/779/2/127)
- Conroy, C., Gunn, J. E., & White, M. 2009, *ApJ*, 699, 486, doi: [10.1088/0004-637X/699/1/486](https://doi.org/10.1088/0004-637X/699/1/486)
- Contini, E., De Lucia, G., Hatch, N., Borgani, S., & Kang, X. 2016, *MNRAS*, 456, 1924, doi: [10.1093/mnras/stv2852](https://doi.org/10.1093/mnras/stv2852)

- Dijkstra, M. 2014, PASA, 31, e040, doi: [10.1017/pasa.2014.33](https://doi.org/10.1017/pasa.2014.33)
- Endsley, R., & Stark, D. P. 2022, MNRAS, 511, 6042, doi: [10.1093/mnras/stac524](https://doi.org/10.1093/mnras/stac524)
- Foreman-Mackey, D., Hogg, D. W., Lang, D., & Goodman, J. 2013, PASP, 125, 306, doi: [10.1086/670067](https://doi.org/10.1086/670067)
- Foreman-Mackey, D., Sick, J., & Johnson, B. 2014, doi: [10.5281/zenodo.12157](https://doi.org/10.5281/zenodo.12157)
- Fukugita, M., Ichikawa, T., Gunn, J. E., et al. 1996, AJ, 111, 1748, doi: [10.1086/117915](https://doi.org/10.1086/117915)
- Haiman, Z., & Loeb, A. 1997, ApJ, 483, 21, doi: [10.1086/304238](https://doi.org/10.1086/304238)
- Harikane, Y., Ouchi, M., Ono, Y., et al. 2019, ApJ, 883, 142, doi: [10.3847/1538-4357/ab2cd5](https://doi.org/10.3847/1538-4357/ab2cd5)
- Hoag, A., Bradač, M., Huang, K., et al. 2019a, ApJ, 878, 12, doi: [10.3847/1538-4357/ab1de7](https://doi.org/10.3847/1538-4357/ab1de7)
- . 2019b, ApJ, 878, 12, doi: [10.3847/1538-4357/ab1de7](https://doi.org/10.3847/1538-4357/ab1de7)
- Ishigaki, M., Ouchi, M., & Harikane, Y. 2016, ApJ, 822, 5, doi: [10.3847/0004-637X/822/1/5](https://doi.org/10.3847/0004-637X/822/1/5)
- Laporte, N., Zitrin, A., Dole, H., et al. 2022, A&A, 667, L3, doi: [10.1051/0004-6361/202244719](https://doi.org/10.1051/0004-6361/202244719)
- Laporte, N., Ellis, R. S., Boone, F., et al. 2017, ApJL, 837, L21, doi: [10.3847/2041-8213/aa62aa](https://doi.org/10.3847/2041-8213/aa62aa)
- Laporte, N., Katz, H., Ellis, R. S., et al. 2019, MNRAS, 487, L81, doi: [10.1093/mnras/slz094](https://doi.org/10.1093/mnras/slz094)
- Lotz, J. M., Koekemoer, A., Coe, D., et al. 2017, ApJ, 837, 97, doi: [10.3847/1538-4357/837/1/97](https://doi.org/10.3847/1538-4357/837/1/97)
- Mason, C. A., & Gronke, M. 2020, MNRAS, 499, 1395, doi: [10.1093/mnras/staa2910](https://doi.org/10.1093/mnras/staa2910)
- Mason, C. A., Trenti, M., & Treu, T. 2022, arXiv e-prints, arXiv:2207.14808. <https://arxiv.org/abs/2207.14808>
- Mason, C. A., Treu, T., Dijkstra, M., et al. 2018, ApJ, 856, 2, doi: [10.3847/1538-4357/aab0a7](https://doi.org/10.3847/1538-4357/aab0a7)
- Mason, C. A., Fontana, A., Treu, T., et al. 2019, MNRAS, 485, 3947, doi: [10.1093/mnras/stz632](https://doi.org/10.1093/mnras/stz632)
- Merlin, E., Bonchi, A., Paris, D., et al. 2022, ApJL, 938, L14, doi: [10.3847/2041-8213/ac8f93](https://doi.org/10.3847/2041-8213/ac8f93)
- Mesinger, A., & Furlanetto, S. 2007, ApJ, 669, 663, doi: [10.1086/521806](https://doi.org/10.1086/521806)
- Mesinger, A., Greig, B., & Sobacchi, E. 2016, MNRAS, 459, 2342, doi: [10.1093/mnras/stw831](https://doi.org/10.1093/mnras/stw831)
- Miralda-Escudé, J. 1998, ApJ, 501, 15, doi: [10.1086/305799](https://doi.org/10.1086/305799)
- Mo, H. J., & White, S. D. M. 1996, MNRAS, 282, 347, doi: [10.1093/mnras/282.2.347](https://doi.org/10.1093/mnras/282.2.347)
- Morishita, T., D’Amato, Q., Abramson, L. E., et al. 2021, ApJ, 908, 163, doi: [10.3847/1538-4357/abd800](https://doi.org/10.3847/1538-4357/abd800)
- Morishita, T., & Stiavelli, M. 2022, arXiv e-prints, arXiv:2207.11671. <https://arxiv.org/abs/2207.11671>
- Morishita, T., Abramson, L. E., Treu, T., et al. 2019, ApJ, 877, 141, doi: [10.3847/1538-4357/ab1d53](https://doi.org/10.3847/1538-4357/ab1d53)
- Oke, J. B., & Gunn, J. E. 1983, ApJ, 266, 713, doi: [10.1086/160817](https://doi.org/10.1086/160817)
- Osterbrock, D. E. 1989, Astrophysics of gaseous nebulae and active galactic nuclei
- Overzier, R. A., Guo, Q., Kauffmann, G., et al. 2009, MNRAS, 394, 577, doi: [10.1111/j.1365-2966.2008.14264.x](https://doi.org/10.1111/j.1365-2966.2008.14264.x)
- Postman, M., Coe, D., Benítez, N., et al. 2012, ApJS, 199, 25, doi: [10.1088/0067-0049/199/2/25](https://doi.org/10.1088/0067-0049/199/2/25)
- Roberts-Borsani, G., Morishita, T., Treu, T., et al. 2022a, ApJL, 938, L13, doi: [10.3847/2041-8213/ac8e6e](https://doi.org/10.3847/2041-8213/ac8e6e)
- Roberts-Borsani, G., Treu, T., Chen, W., et al. 2022b, arXiv e-prints, arXiv:2210.15639. <https://arxiv.org/abs/2210.15639>
- Roberts-Borsani, G., Treu, T., Mason, C., et al. 2022c, arXiv e-prints, arXiv:2207.01629. <https://arxiv.org/abs/2207.01629>
- Robertson, B. E., Furlanetto, S. R., Schneider, E., et al. 2013, ApJ, 768, 71, doi: [10.1088/0004-637X/768/1/71](https://doi.org/10.1088/0004-637X/768/1/71)
- Shull, J. M., Harness, A., Trenti, M., & Smith, B. D. 2012, ApJ, 747, 100, doi: [10.1088/0004-637X/747/2/100](https://doi.org/10.1088/0004-637X/747/2/100)
- Steinhardt, C. L., Jauzac, M., Acebron, A., et al. 2020, ApJS, 247, 64, doi: [10.3847/1538-4365/ab75ed](https://doi.org/10.3847/1538-4365/ab75ed)
- Tegmark, M., Silk, J., Rees, M. J., et al. 1997, ApJ, 474, 1, doi: [10.1086/303434](https://doi.org/10.1086/303434)
- Tilvi, V., Malhotra, S., Rhoads, J. E., et al. 2020, ApJL, 891, L10, doi: [10.3847/2041-8213/ab75ec](https://doi.org/10.3847/2041-8213/ab75ec)
- Trenti, M., Santos, M. R., & Stiavelli, M. 2008, ApJ, 687, 1, doi: [10.1086/592037](https://doi.org/10.1086/592037)
- Trenti, M., Bradley, L. D., Stiavelli, M., et al. 2012, ApJ, 746, 55, doi: [10.1088/0004-637X/746/1/55](https://doi.org/10.1088/0004-637X/746/1/55)
- Treu, T., Schmidt, K. B., Brammer, G. B., et al. 2015, ApJ, 812, 114, doi: [10.1088/0004-637X/812/2/114](https://doi.org/10.1088/0004-637X/812/2/114)
- Treu, T., Roberts-Borsani, G., Bradac, M., et al. 2022, ApJ, 935, 110, doi: [10.3847/1538-4357/ac8158](https://doi.org/10.3847/1538-4357/ac8158)
- Zheng, W., Shu, X., Moustakas, J., et al. 2014, ApJ, 795, 93, doi: [10.1088/0004-637X/795/1/93](https://doi.org/10.1088/0004-637X/795/1/93)